Water Supply

IWA PUBLISHING

Water Supply Vol 22 No 1, 574 doi: 10.2166/ws.2021.253

Numerical investigation of flow field around T-shaped spur dyke in a reverse-meandering channel

Ravi Prakash Tripathi* and K. K. Pandey

Department of Civil Engineering, IIT-BHU, Varanasi, India
*Corresponding author. E-mail: ravipt.rs.civ15@itbhu.ac.in

ABSTRACT

In this paper, the flow characteristics around T-shape spur dyke situated in the reverse meandering channel with a rigid bed is simulated using renormalization group (RNG) $k-\varepsilon$ turbulence model with ANSYS 2018 Fluent software. To solve the model in 3D ways we used Navier-Stroke's equation based on the principle of conservation of mass and momentum within a moving fluid. For studying the flow characteristics, computational fluid dynamics were applied with all geometric parameters and the turbulence was simulated using (RNG) $k-\varepsilon$ equations of model. In this simulation, the structured meshes were used with different diameters and diameters of meshes are high at the exit channel for obtaining accuracy in the result. In this study, we mainly focus on the effect of Froude number on flow pattern and several other characteristics like velocity distribution, flow separation, bed-shear-stress distribution. The final result of this research work is compared with the condition when no structure is present in the channel.

Key words: channel bend, flow field, meandering channel, scour, spur dyke, turbulence model

HIGHLIGHTS

- A numerical investigation is carried out to study the flow field characteristics around a T-shaped spur dike located in a reverse meandering channel with rigid bed.
- RNG $k-\varepsilon$ turbulence model is implemented using ANSYS fluent software.
- Study the effect of Froude number on flow pattern, several characteristics.
- The results are then compared with the condition when no structure is placed.

GRAPHICAL ABSTRACT

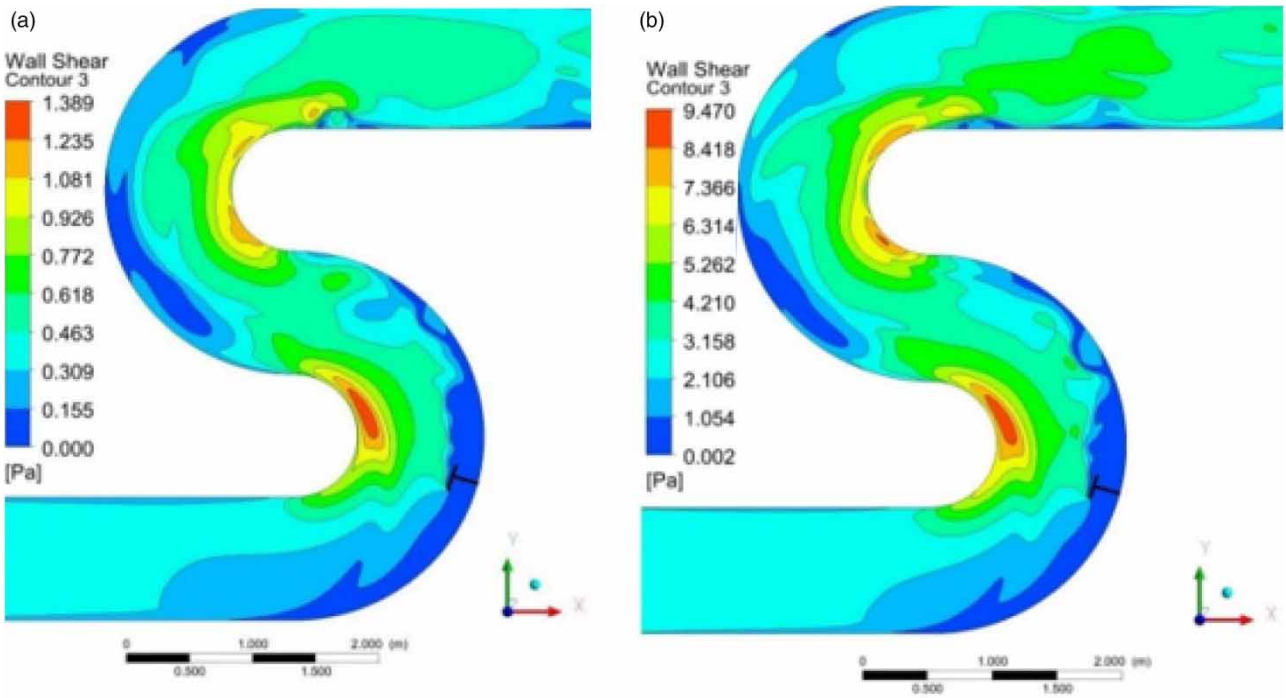

INTRODUCTION

The flow in a river bend or meandering channel is highly turbulent and stormy due to continuous change in the curvature of banks and high topography irregularities (Pu *et al.* 2020, 2021). The flow pattern in a curved channel consists of spiral flow between the river bed and water surface, transverse rotational flow generated by the centrifugal force in bend, secondary flow, and so on (Pandey *et al.* 2018a, 2018b, Singh *et al.* 2019). It causes heavy bank erosion resulting in its lateral migration. Rozovski (1957) studied and discussed the flow characteristics and boundary shear-stress distribution in a curved channel. Yen (1967) experimented with flow pattern and bed configuration in a meandering channel under subcritical flow conditions. Naji *et al.* (2010) worked on the flow pattern in a 90-degree channel bend and observed that the flow in the bend is highly influenced by secondary flow and centrifugal force. They further observed that the flow near the channel orients towards the inner bank shifts to the outer bank near the water surface. Vaghefi *et al.* (2016a, 2016b) conducted experiments in a 180-degree channel bend and analyzed the effect of flow characteristics on bed shear-stress distribution.

To prevent bank erosion in the curved channel, spur dykes are constructed across the channel width extending from the outer bank into the river. Spur dyke restricts the water flow and hence ensures deepening of the main channel. This can be used for navigation purposes, uniform discharge into an irrigation channel, and rehabilitation of flood plain. Despite its significant use, the study on spur dyke present in channel bend is still limited (Fazli *et al.* 2008; Vaghefi *et al.* 2019). The majority of studies in this field have been carried out in a straight channel such as Kothyari & Ranga Raju (2001), Jennifer *et al.* (2011), Jiao *et al.* (2017), Kuhnle & Alonso (2013), Pandey *et al.* (2018a, 2019, 2020, 2021), Pourshahbaz *et al.* (2020), Singh *et al.* (2020), Xiufang *et al.* (2012) and so on. The flow past a spur dyke present at the channel bend or meander is highly turbulent, leading to the formation of local scour, which further increases with increasing scour depth. Therefore, it becomes essential to evaluate the flow behavior around the spur dyke. In general, the flow regime is divided into two zones, wake-up and mixing zones around a spur. The flow characteristics around spur dyke include the formation of secondary flow, vortices, down flow, flow, turbulence, and so on (Zhang & Nakagawa 2008; Pandey *et al.* 2018a, 2021). The current experimental and numerical studies conducted on spur dyke present in a channel bend (mainly 90-degree and 180-degree) or a meander to evaluate the inference of several important

parameters on local scour. These parameters include upstream Froude number, submergence ratio, and geometry of channel spur dyke, bed configuration, etc.

Giri *et al.* (2004) developed the 2D numerical model using a cubic-interpolated pseudoparticle (CIP) numerical technique to study the flow field and turbulence around spur dykes located in a rigid bed meandering channel. Sharma & Mohapatra (2012) experimented with a rigid bed sinusoidal meandering channel with trapezoidal cross-section and fined the dimensions of separation zone (length and width). This is highly influenced by the position of structure in the channel that varies from 4.0 to 22.8 times the spur dyke length; however, it remains nearly unchanged under varying discharge. The same results were also reported in a spur dyke positioned in a straight channel (Yazdi *et al.* 2010).

Fazli *et al.* (2008) discuss as the spur dyke shift far from the entry of the bend, the depth of scour and the intensity of the flow increased in a 90-degree channel bend. The separation zone of the vortex expands with an increase in the wing length of the spur dyke, and the vortex with the anti-clock direction was formed both upstream and downstream of the spur dyke Ghodsian & Vaghefi (2009). In addition, a vortex with a clockwise direction is also formed between wings of spur dyke in the channel walls downstream. For a single T-shaped spur dyke located at an angle of 75-degrees (from the entry) in a 90-degree bend, the strength of secondary flow and vorticity gradually increases from the beginning of the bend to maximum value at section 74-degrees. It then decreases until the exit of the bend (Vaghefi *et al.* 2017). Therefore, it says that these vortices might be formed due to interaction between the longitudinal velocity component of flow and secondary flow. Salamatian *et al.* (2016) at a 90-degree channel bend with three spur dykes placed in 5-degree consecutive angular spacing along the bend. The position of the first spur dyke (from the entry of bend) was kept at 30-degrees, 45-degrees, and 60-degrees. This study shows that shifting the spur dykes downstream decreases the length of the separation zone while the width remains constant, increasing the bed-shear-stress.

Naji *et al.* (2010) prove with their experiment that SSIIM (Sediment Simulation in Intakes with Multiblock option) model can be used to simulate the flow pattern accurately in a 90-degree bend (without any structure). Olsen (2018) investigated the variation of flow velocity, which implements $k-\varepsilon$model to solve Navier-Stokes's equations in a non-orthogonal grid. Acharya & Duan (2011) implemented the FLOW-3D model to simulate the flow field around a series of three spur dykes using several turbulence models such as renormalization group (RNG) $k-\varepsilon$ model, standard two-equation $k-\varepsilon$ model, mixing length model, and large eddy simulation (LES) model. They noticed that none of the models is accurately able to predict the turbulence properties. However, the RNG $k-\varepsilon$ model can predict the mean velocities and hence recommend the same. Kafle (2013) uses a 2D numerical model with CIP techniques to simulate flow field in spur dyke present at 90-degree channel bend. The turbulence models such as $k-\varepsilon$ model, zero equation models, and constant eddy viscosity model were implemented and compared. Vaghefi *et al.* (2014) studied RNG $k-\varepsilon$ turbulence numerical model FLOW-3D to investigate how the change in Fr number influences flow pattern past a T-shaped spur dyke at a bend angle of 45-degrees (measured from the entry) in a 90-degree bend and estimate as the Froude number increases from 0.2 to 0.6, vertical velocity component of flow increases by about two times, and the distance between return flow and web wing of spur dyke increases by 10 times. Radan & Vaghefi's (2016) study with SSIIM model simulates the submergence on flow and scour pattern around a spur dyke at 45-degrees (from the entry) and 90-degree bend, proposed that with an increase in submergence of the spur dyke, the distance of vortices with a horizontal axis from the structure decreases.

On the other hand, the distance of vortices with the vertical axis from the spur dyke decreases upstream remains unchanged downstream.Similar work done with the same numerical model but only at 90-degree, discussing the secondary flow strength and flow separation around attractive, vertical, and repelling T-shaped spur dykes seems that the secondary flow is higher for attractive than repelling. The separation zone increases with a rise in water elevation Vaghefi *et al.* (2019).

From the literature survey, most researches have been conducted in a 90-degree channel bend; researches including other curved channels such as 180-degree bend and meandering channel have been either neglected or limited. In hydraulic engineering, soft computing and numerical methods have been widely used and successfully simulated hydraulic parameters (Samadi *et al.* 2015, 2021). Therefore, this paper investigates the flow pattern numerically in a reverse meandering channel near the spur dyke with a rigid bed under subcritical conditions. It also includes the effect of the Froude number on the flow pattern. The results are then compared with that under the condition when no structure is located in the channel. A numerical investigation was carried out using ANSYS fluent software. The results include streamlines, velocity distribution, flow separation, and bed-shear-stress distribution.

NUMERICAL MODELING

Equation formation

Computational Fluid Dynamics (CFD) involves solving Navier-Stroke's equation based on the principle of conservation of mass and momentum within a moving fluid. In general, the conservation of mass and momentum in differential equation form is described by Equations (1) and (2), respectively.

$$\frac{\partial \rho}{\partial t} + \nabla \cdot (\rho \vec{v}) = 0 \tag{1}$$

$$\frac{\partial}{\partial t}(\rho \vec{v}) + \nabla \cdot (\rho \vec{v}\vec{v}) = -\nabla \mathrm{p} - \nabla \cdot [\mu(\nabla \vec{v} + \nabla \vec{v}^{T})] + \rho \vec{\mathrm{g}} + \vec{\mathrm{F}} \tag{2}$$

Here, ρ = density of the fluid, $\vec{v}$ = velocity of moving fluid at time t, p = pressure, $\vec{\mathrm{g}}$ = acceleration due to gravity, $\vec{\mathrm{F}}$ = body force, $\mu = \mu_o + \mu_t$ where, μ_o = viscosity of the fluid, and μ_t = turbulence viscosity. The RNG $k-\varepsilon$ model (Yakhot *et al.* 1992; Yazdi *et al.* 2010) was used to determine the turbulence viscosity term in Equation (2). The turbulence viscosity is modeled as

$$\mu_t = \rho C_\mu \frac{k^2}{\epsilon} \tag{3}$$

where, $C_\mu = 0.0845$ (a constant), k and ϵ are turbulence kinetic energy, and energy-dissipation rate, respectively. The k and ϵ terms in Equation (3) are obtained from the following two transport equations.

$$\frac{\partial}{\partial t}(\rho k) + \nabla \cdot (\rho k \vec{v}) = \nabla \cdot \left[\left(\mu + \frac{\mu_t}{\sigma_k}\right)\nabla k\right] + \mathrm{G}_k - \rho\epsilon \tag{4}$$

$$\frac{\partial}{\partial t}(\rho \epsilon) + \nabla \cdot (\rho \epsilon \vec{v}) = \nabla \cdot \left[\left(\mu + \frac{\mu_t}{\sigma_\epsilon}\right)\nabla \epsilon\right] + C_{1\epsilon}\frac{\epsilon}{k}\mathrm{G}_k - C_{2\epsilon}^{*}\rho\frac{\epsilon^2}{k} \tag{5}$$

where

$$C_{2\epsilon}^{*} = C_{2\epsilon} + \frac{C_\mu \eta^3}{1+\beta\eta^3}\left[1 - \frac{\eta}{\eta_0}\right] \tag{6}$$

Here, G_k represents the production of turbulence kinetic energy given by $\mathrm{G}_k = \mu_t S^2$, $\eta = Sk/\epsilon$, S = modulus of the mean rate of strain tensor; σ_k and σ_ϵ are the turbulent Prandtl numbers; and C_μ, $C_{1\epsilon}$, $C_{2\epsilon}$, η_0, and β are constants. The value of constants in the RNG $k-\varepsilon$ model is listed in Table 1.

The RNG $k-\varepsilon$ model was developed using the RNG method to normalize the Navier-Stokes equation to account for even small scales of fluid motion. Therefore, it makes RNG $k-\varepsilon$ model a suitable choice to model turbulence flow around the spur dyke. In this paper, ANSYS fluent software (ANSYS 2018) was used to simulate the flow around the spur dyke located in a reverse-meandering channel.

Experimental setup introduction

In this study, the reverse-meandering channel consists of two consecutive bends in reverse order. These bends were connected with the straight inlet and outlet channels, each of length 4.0 m. The channel's cross-section was kept prismatic with a uniform width of 1.0 m and depth of 0.2 m. The central radius of bends was designed as 1.0 m. Since the relative

Table 1 | Value of constants in RNG $k-\varepsilon$ model

C_μ	$C_{1\epsilon}$	$C_{2\epsilon}$	σ_k	σ_ϵ	η_0	β
0.0845	1.42	1.68	0.7194	0.7194	4.38	0.012

curvature was 1.0, such a bend is categorized as a sharp bend. The central angle of the bend was kept at 180 degrees for the maximum deflection of flow and hence, to generate full development of secondary circulation. Here, two cases were considered: (1) when no spur dyke was located in the bend; and (2) when a T-shaped spur dyke was located at the outer bank of the first bend. For case 2, the spur dyke had a thickness of 0.01 m (or 10 mm) and height of 0.20 m and was placed at an angle of 75-degrees (measured from entry to the first bend). The spur dyke length and wing length were kept at 0.2 m (i.e., 20% of channel width). A schematic diagram for case 2 is shown in Figure 1. The CAD model for both cases was prepared in Solid Works, which were imported in ANSYS fluent for further processing.

By default, unstructured meshing is available in ANSYS fluent (ANSYS 2018), and the same was used in the present research of the complex geometry near the spur dyke. The flow simulation was iterated for several mesh configurations of progressive fine sizes to obtain the most accurate results under identical flow conditions. A mesh system was then considered, which had a negligible effect on computational results while reducing the simulation (model run) time. For case 1, uniform mesh sizes of 20 and 40 mm were used to discretize bends and inlet, and straight outlet reaches, respectively, and for case 2, a uniform mesh size of 20 mm was used in general, while a denser mesh size of 10 mm was used near the spur dyke. Some of the common parameters of volume meshing are listed in Table 2. The volume meshing for both cases is shown in Figure 2.

The flow velocity inlet and pressure outlet were introduced at the entry and exit of the computational domain, respectively. The banks of the channel were defined as a wall with no-slip and standard wall roughness conditions. The empirical standard wall function (Spalding 1974) was used to estimate the effect of the wall on the flow field. The channel bed was rigid, and hence, treated as a wall. At the same time, the water surface exposed to the environment above was assumed to be symmetrical, which enforces zero normal flow velocity and shear-stress. The boundary conditions for computation are shown in Figure 1 (marked in rectangular box).

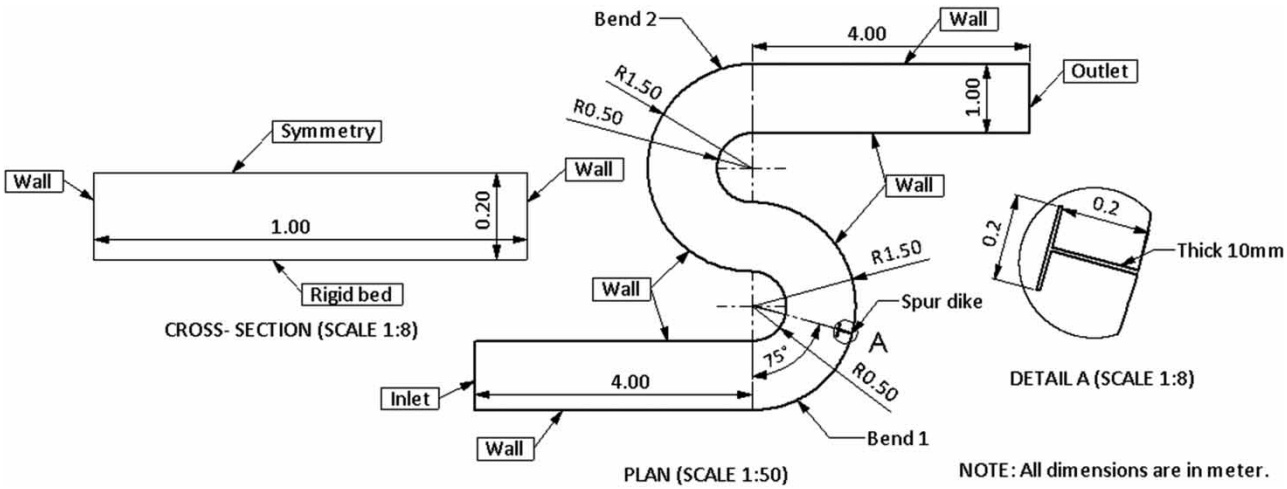

Figure 1 | Numerical model for case 2 (i.e., spur dyke located at 75-degrees).

Table 2 | Some general parameters of volume meshing used

S.No.	Parameters	Case 1: With no spur dyke	Case 2: With spur dyke
1	Number of nodes	3,51,450	8,29,840
2	Number of mesh elements	31,260	7,76,559
3	Size of mesh elements	20–40 mm	10–20 mm
4	Type of mesh elements	Hexahedral	Hexahedral with few tetrahedral
5	Average mesh quality	0.9663	0.7131
6	Size function	Curvature	Proximity and curvature

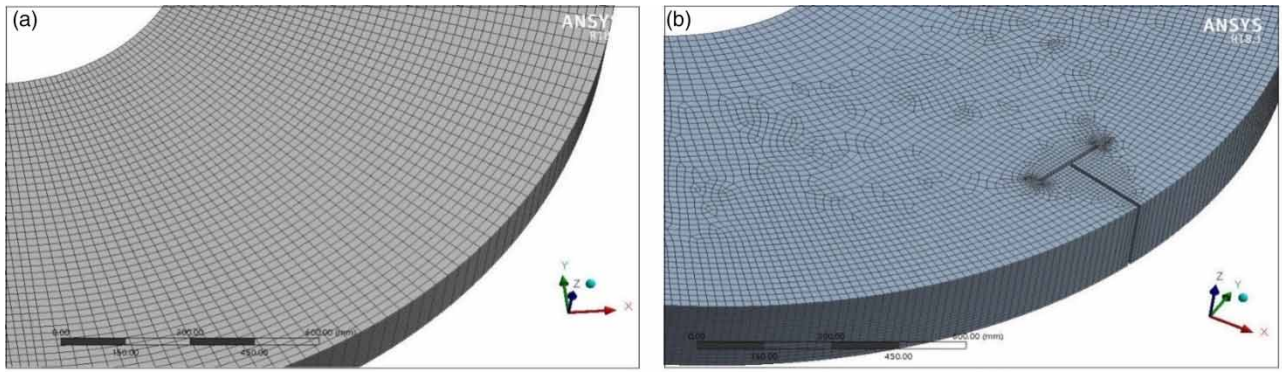

Figure 2 | Computational mesh grid for (a) case 1: without spur dyke, and (b) case 2: with spur dyke.

To solve the numerical model, a pressure-velocity coupling-based SIMPLE scheme was implemented. SIMPLE scheme stands for semi-implicit method for pressure linked equations, which uses the relationship between pressure and velocity corrections to obtain pressure field and to enforce the law of conservation of mass (ANSYS 2018). A steady-state simulation was performed for each case with five different approaching flow conditions, i.e., Froude number equal to 0.29, 0.43, 0.57, 0.71, and 0.86 (subcritical flow condition).

RESULTS AND DISCUSSION

Velocity distribution

Figures 3 and 4 show the velocity contour at 25% and 75% water depth for case 1 (i.e., when no spur dyke is located in the bend), at Froude numbers equal to 0.29 and 0.86, respectively. From the figures, it is clear that the velocity distribution shows a similar trend for all Froude numbers; only intensity and magnitude increase with increasing Froude number. In general, the flow velocity increases as one gradually moves from the concave side (outer bank) to the convex side (inner bank). The local maximum velocity occurs at the convex tips in both bends. Due to secondary flow formation, the lateral velocity component (across channel width) contributes significantly to the maximum velocity. However, secondary flow strength is relatively higher in the second bend due to a change in curvature of bank and flow direction as the flow enters the second bend. Hence, the maximum velocity at the convex tip of the second bend is greater than that of the first bend, as seen from the velocity streamline in Figure 5. In the vertical direction, the velocity increases from channel bed to water surface.

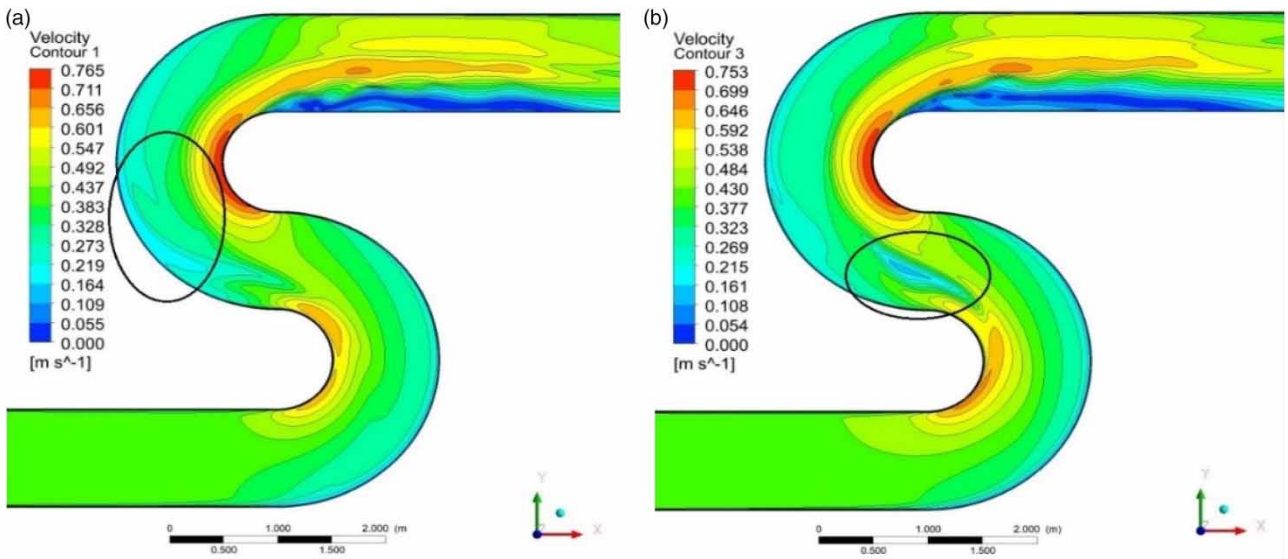

Figure 3 | Velocity contour for case 1 (without spur dyke) for Froude number = 0.29 at (a) 25%; and (b) 75% of water depth.

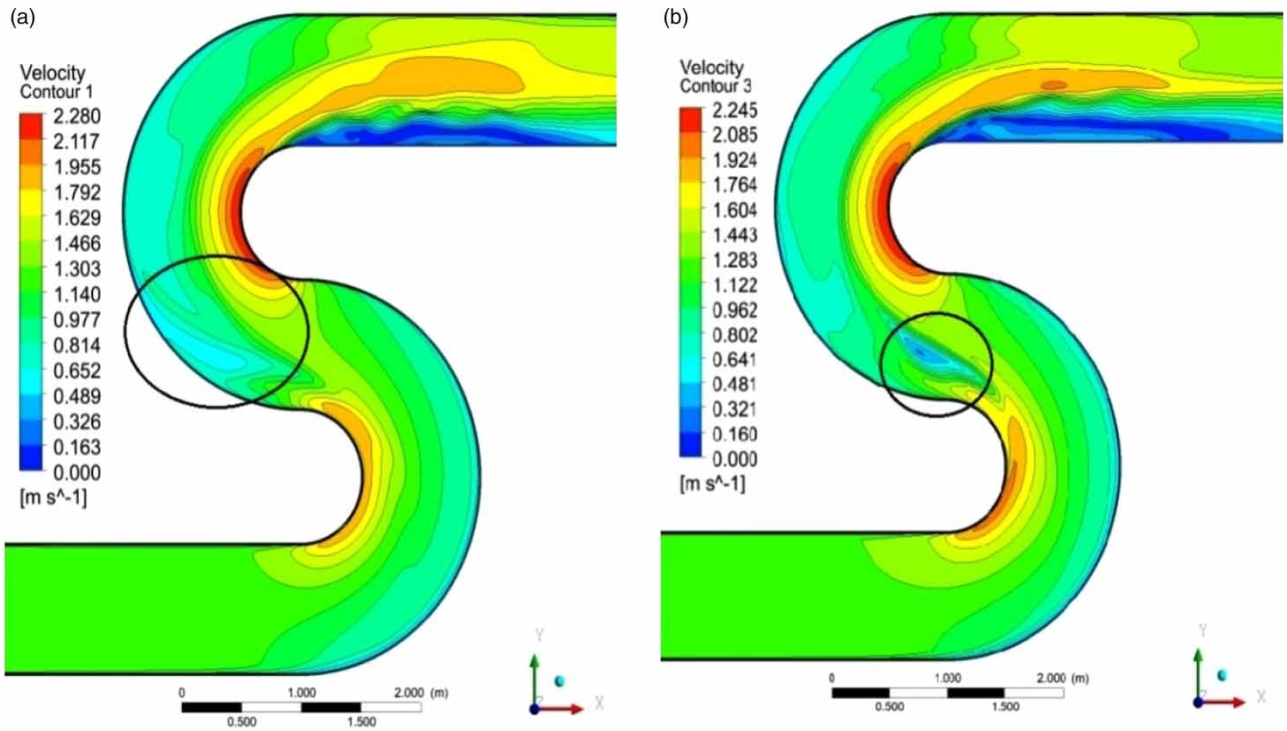

Figure 4 | Velocity contour for case 1 (without spur dyke) for Froude number = 0.86 at (a) 25%; and (b) 75% of water depth.

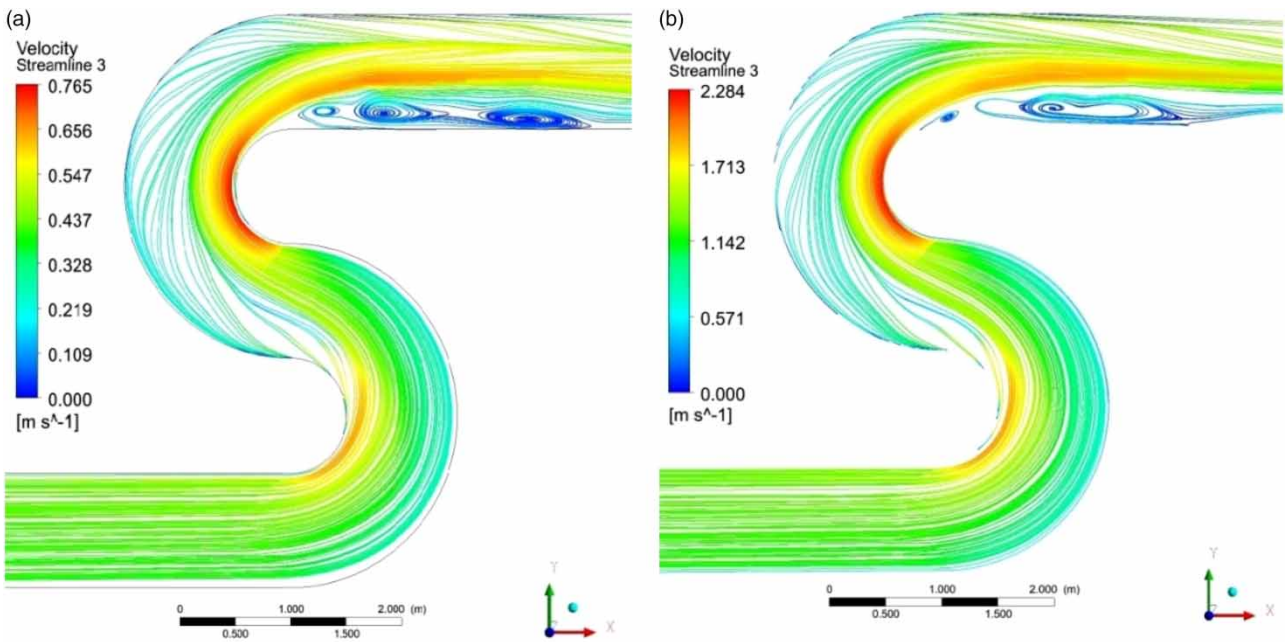

Figure 5 | Velocity streamline for case 1 (without spur dyke) at 75% of water depth for Froude number = (a) 0.29; and (b) 0.86.

In the presence of spur dyke (case 2), the velocity distribution shows significant changes, which become more prominent with increasing Froude number. Similar to case 1, the flow velocity increases from the inner bank to the outer bank in both the bends, as shown in Figures 6 and 7. The obstruction to flow caused by the spur dyke increases the mean flow velocity,

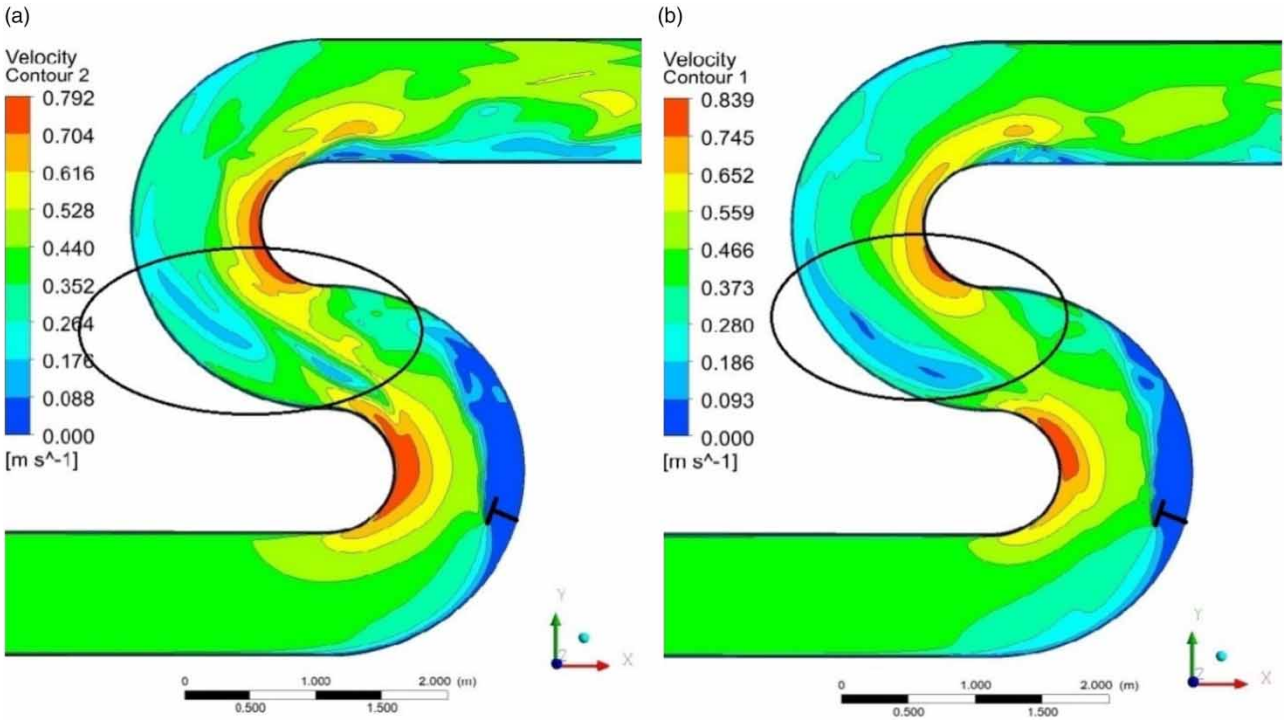

Figure 6 | Velocity contour for case 2 (with spur dyke) for Froude number = 0.29 at (a) 25%; and (b) 75% of water depth.

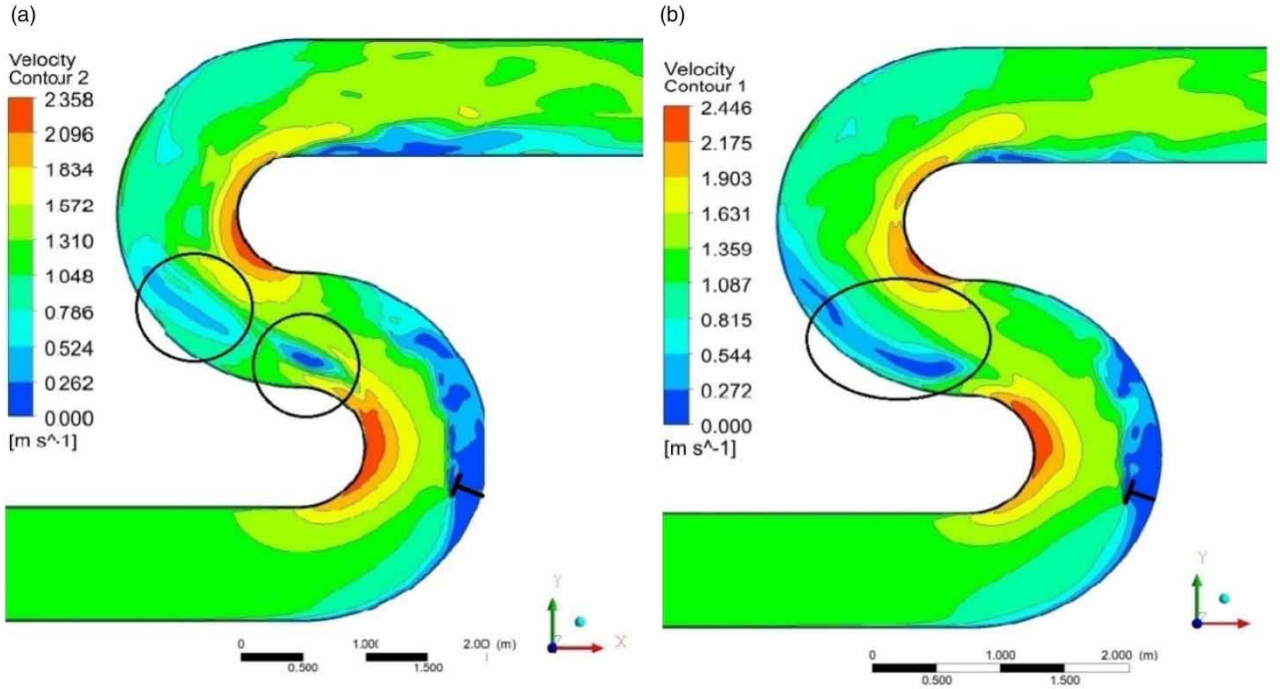

Figure 7 | Velocity contour for case 2 (with spur dyke) for Froude number = 0.86 at (a) 25%; and (b) 75% of water depth.

extending downstream from its location due to channel width contraction. Similar to case 1, the local maximum velocity is found near the convex tip (inner bank) in each bend. However, the global maximum flow velocity shifts to the convex tip of the first bend.

In the absence of the spur dyke (case 1), a low or zero velocity zone forms at the junction of two bends. The zone gets well-defined as one moves from channel bed to water surface. At a high Froude number, it becomes localized (or shrinks or converges) at the junction. Near the channel, it extends downstream along the outer bank of the second bend. It is marked with a circle in Figures 3 and 4. It occurs due to the convolution of flow reflected from the outer bank (secondary flow) and flows separate at the inner bank of the first bend (see Figure 5).

In the presence of the spur dyke (case 2), there is the formation of two such low or zero velocity zones, one near the junction of two bends and the other at the outer bank of the second bend (see Figures 6 and 7). Similar to the previous case, these zones become well-defined near the water surface and at a higher Froude number.

The 3D flow characteristics around the spur dyke (case 2) include upflow, downflow, vortices, and so on, as shown in Figures 8 and 9. At location of 50% of spur dyke length from the outer bank of the first bend, a total of three vortices having a horizontal axis of rotation are formed around the spur dyke. Two vortices with anti-clockwise direction formed close to the spur dyke, upstream and downstream, and another vortex with clockwise direction formed relatively far away from spur dyke downstream. With the increase in Froude number, these vortices shift downward and show an increase in their strength as well (see Figures 8(a) and 9(a)). At the location, 100% of spur dyke length from the outer bank of the first bend (or along the wing length of spur dyke), a vortex with anti-clockwise direction is observed at the upstream end of the spur dyke, while several vortices are observed at its downstream end. At downstream of the spur dyke, a vortex with clockwise direction is formed at the mid-water depth, which eventually dies off at higher Froude number; however, a vortex with anti-clockwise direction is observed near the channel bed, which shifts towards the spur dyke at higher Froude number, probably caused due to strong a returning flow (see Figures 8(b), and 9(b)).

Flow separation zone

At the upstream, the flow streamline starts to get separated from the boundary (i.e. channel bank) as it approaches the spur dyke. This zone is called the separation zone. The flow streamline then reattaches to the channel bank at the downstream, causing the formation of reattachment zone. A schematic diagram of flow separation is shown in Figure 10. In the figure, separation zone and reattachment zone lengths are represented by '*m*' and '*n*', respectively.

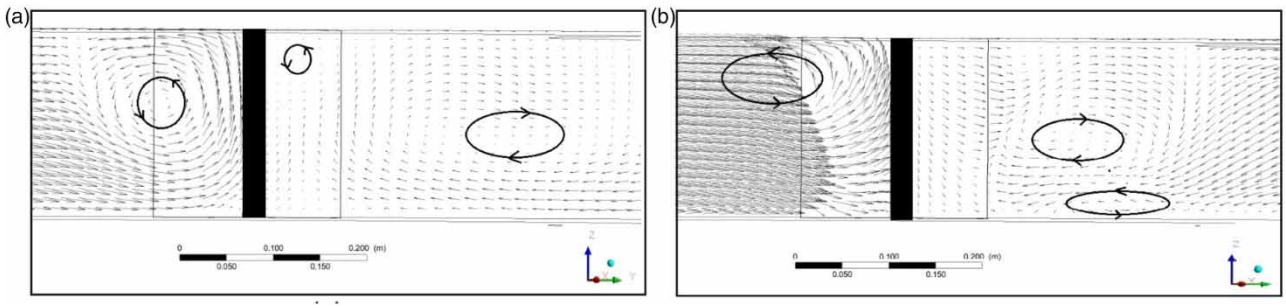

Figure 8 | Flow velocity vector around spur dyke (case 2) for Froude number = 0.29 at location (a) 50% of spur dyke length from the outer bank of first bend; and (b) along the spur dyke's wing (or 100%) of spur dyke length.

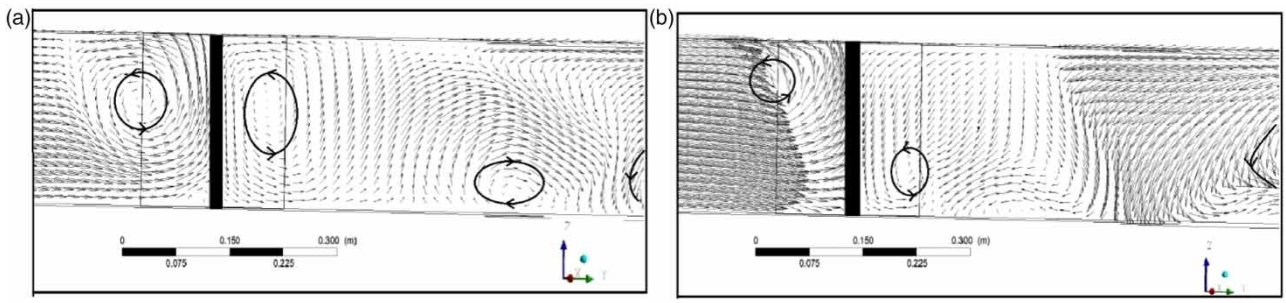

Figure 9 | Flow velocity vector around the spur dyke (case 2) for Froude number = 0.86 at location (a) 50% of spur dyke length from the outer bank of the first bend; and (b) along the spur dyke's wing (or 100%) of spur dyke length.

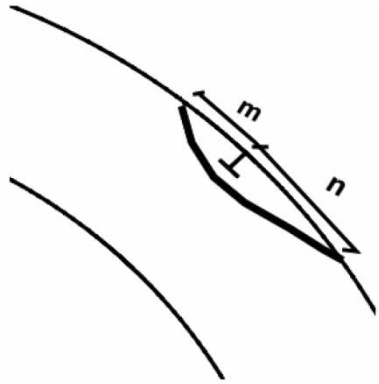

Figure 10 | A schematic diagram of flow separation around spur dyke (*source*: Vaghefi *et al.* 2019).

In case 1 (absence of spur dyke), flow separation starts from the begnining of the straight outlet channel (or end of second bend), and stretches downstream, as can be seen in Figures 3–5. In this case, the flow separation zone length is represented by '$m + n$'. Figure 11 shows the variation of $(m + n)/L$ at various water depth and inflow Froude number. From Figure 11(a), it can be seen that for all values of inflow Froude number, the value of $(m + n)/L$ increases as one moves towards the water surface. The value of $(m + n)/L$ is observed maximum at $Fr = 0.43$, while it remains nearly unaffected at higher Froude number, as can be seen from Figure 11(b). At higher inflow Froude number, the strong secondary flow from the outer bank interacts with longitudinal flow streamlines at the downstream causing reduction in flow separation zone length.

In case 2, the flow separation in straight outlet reach becomes negligible due to reduced velocity caused by the presence of the spur dyke. Table 3 shows the separation zone and reattachment zone length around the spur dyke at two water depth levels. From the table, it is clear that the separation zone length, m/L, remains unaffected by inflow Froude number, while the reattachment zone length, n/L shows slight variation with inflow Froude number. On comparing the values of m/L and n/L at two water depth levels, it is discovered that the m/L remains nearly constant at all water depths, while n/L increases as one moves from channel bed to water surface. A similar observation is made by Vaghefi *et al.* (2019).

Bed-shear-stress distribution

Even though a rigid bed is assumed in this paper, bed-shear-stress distribution can provide a qualitative understanding of scour and sediment transportation in the channel with mobile bed (or live bed condition). In general, the initiation of sediment transport at the channel bed is evaluated using a critical shear-stress threshold (Ouillon & Le Guennec 1996). The shear-stress distribution at the channel bed gives the potential location of sediment erosion and deposition along the channel length. The location characterized by high bed-shear-stress has the potential of bed erosion (or scour) or vice versa.

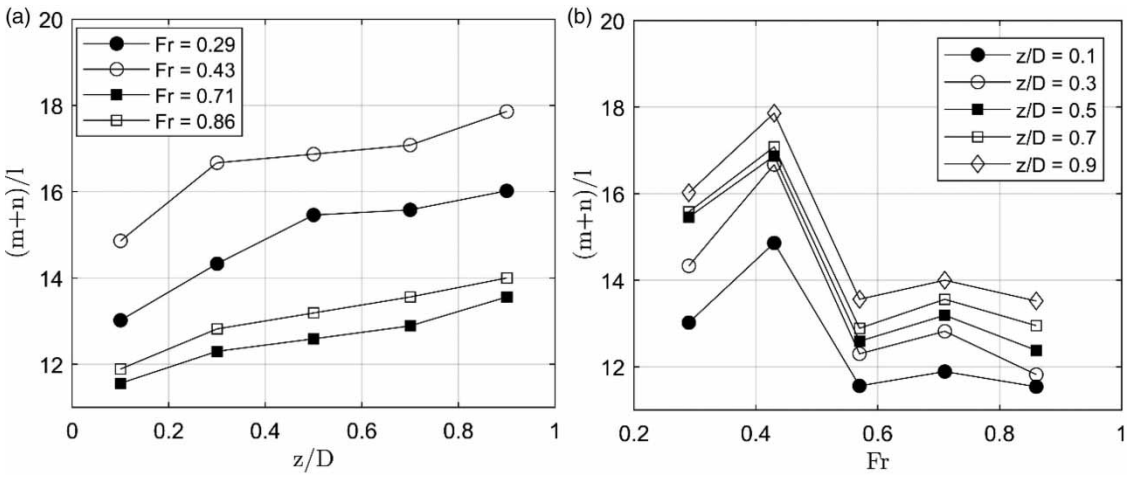

Figure 11 | (a) $(m + n)/L$ vs z/D; and (b) $(m + n)/L$ vs Fr for flow separation in straight outlet channel (case 1).

Table 3 | m/L and n/L values at $z/D = 0.25$ and 0.75 for flow separation around the spur dyke (case 2)

		$z/D = 0.25$		$z/D = 0.75$	
S. no.	*Fr*	m/L	n/L	m/L	n/L
1	0.29	3.28	5.32	3.42	6.37
2	0.43	3.23	5.32	3.30	6.48
3	0.57	3.17	5.31	3.28	6.34
4	0.71	3.20	5.36	3.30	6.46
5	0.86	3.26	5.36	3.36	6.47

In case 1, the bed-shear-stress distribution shows a general trend for all flow conditions. In the absence of a spur dyke, the bed-shear-stress increases as one move from the concave side (outer bank) to the convex side (inner bank). A similar observation was also made by Vaghefi *et al.* (2016a, 2016b) for 180-degree channel bend. It becomes clear from Figure 12 that the bed-shear-stress at the convex tips could potentially result in significant scour in these regions. It occurs due to high flow velocity in these regions, as shown in Figures 12 and 13. However, the maximum bed-shear-stress occurs at the convex tip of the second bend. Due to the formation of high secondary flow in the second bend caused by a reverse flow direction and change in curvature as water enters from bends first to second. The maximum value of bed-shear-stress at these two locations is listed in Table 4. Interestingly, the ratio of shear-stress at the two locations remains nearly constant (equal to 1.38). Further, at the downstream of the second bend (i.e., the straight outlet channel), a high value of bed-shear-stress is observed outside the flow separation zone, which increases drastically with an increase in Froude number, as shown in Figure 13.

In case 2, the bed-shear-stress distribution changes drastically due to a spur dyke in the bend, as shown in Figure 13. However, the general trend of bed-shear remains similar to that in case 1. Due to the presence of the spur dyke, the shear-stress increases in both the bends. However, the location of maximum shear-stress shifts from the convex tip of the second bend to that of the first bend. In this case, the shear-stress ratio at the two locations is equal to 0.89 (a constant). The bed-shear-stress in the separation zone (or recirculation zone) reduces, resulting in a deposition. The same is observed at the concave side (outer bank) of the second bend.

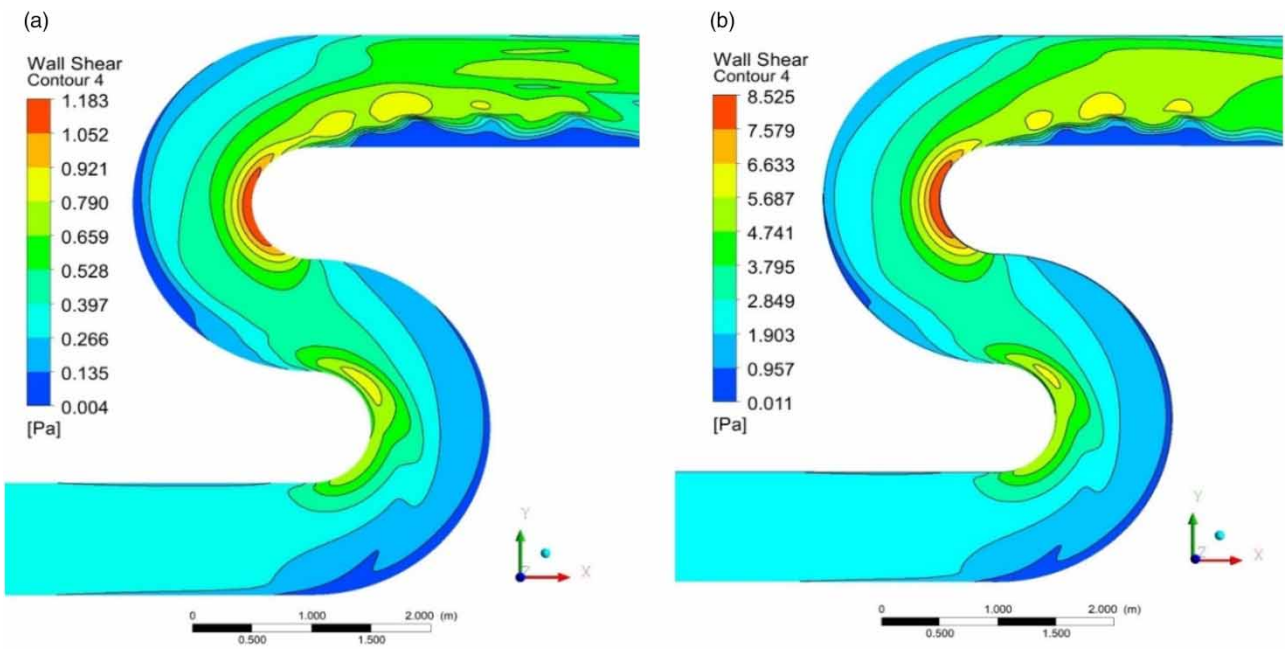

Figure 12 | Bed-shear-stress distribution in case 1 (without spur dyke) for Froude no. = (a) 0.29; (b) 0.86.

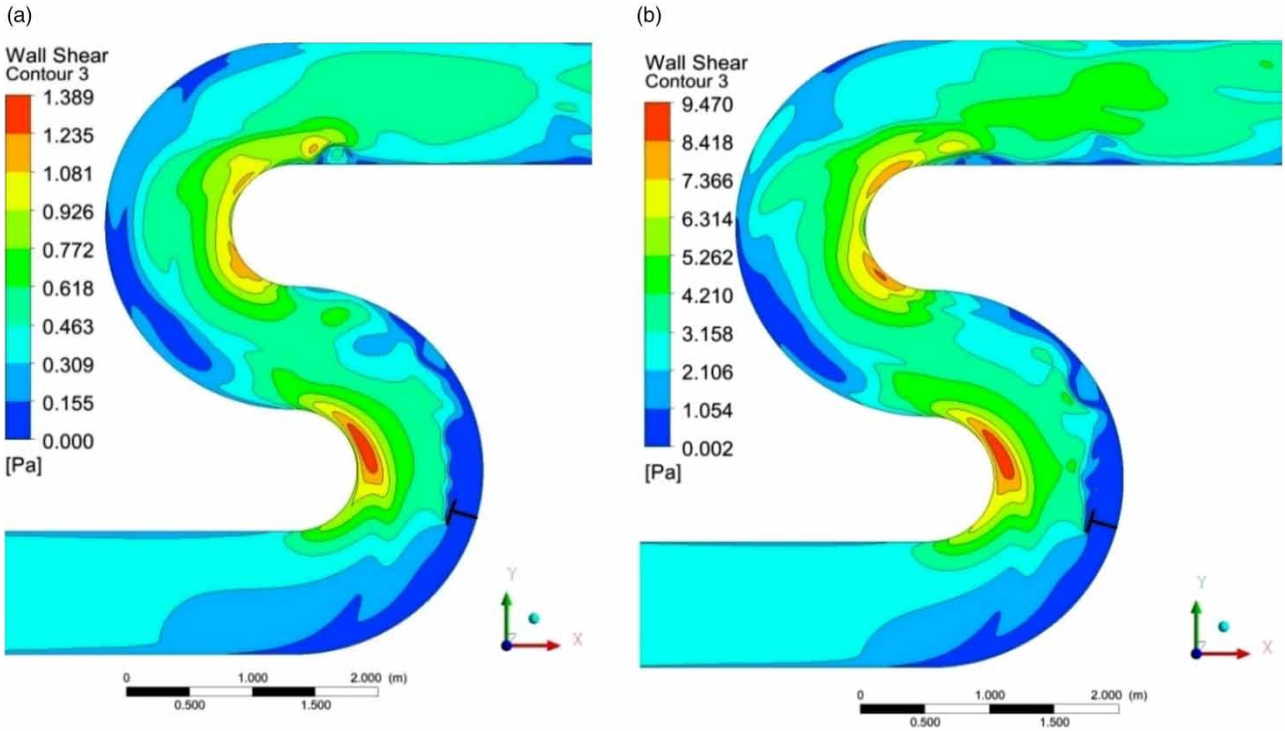

Figure 13 | Bed-shear-stress distribution in case 2 (with spur dyke) for Froude no. = (a) 0.29; (b) 0.86.

Table 4 | Maximum value of bed-shear-stress at the convex tips (side) of bends

		Maximum bed-shear-stress at the convex tips of (N/m^2)			
		Case 1: Without spur dyke		Case 2: With spur dyke	
S. no.	Froude no.	First bend	Second bend	First bend	Second bend
1	0.29	0.856	1.183	1.389	1.235
2	0.43	1.769	2.443	2.789	2.476
3	0.57	2.968	4.108	4.613	4.111
4	0.71	4.435	6.146	6.965	6.196
5	0.86	6.160	8.525	9.472	8.415

Further, the shear-stress value downstream of the second bend also decreases compared to that in case 1 (see Figures 12 and 13). Near the tip of the spur dyke, the bed-shear-stress increases, resulting in bed erosion. In both cases, the shear-stress increases with an increase in Froude number.

Validation

For a particular numerical model to be verified, we compare the variation in the parameter of with and without spur dyke in meandering channel bend at 180-degree with the result of another experimental model under the same condition with other research paper. Present simulations are performed with five different approaching flows under the subcritical condition.

Figures 3 and 4 represent the velocity contour at 25% and 75% depth of water having Froude numbers 0.29 and 0.86 with no structure present in the meander. This velocity shows similar trends with the Froude number.

Figures 7 and 8 show the velocity contour with spur dyke in a meander having water depth of 75% and 0.29 Froude number, and it is clearly shown that from the initial bend to the wings of spur dyke the velocity attended same direction and amount. It is seen that the longitudinal velocity increases at the inner wall but closer to the external bend and vertical

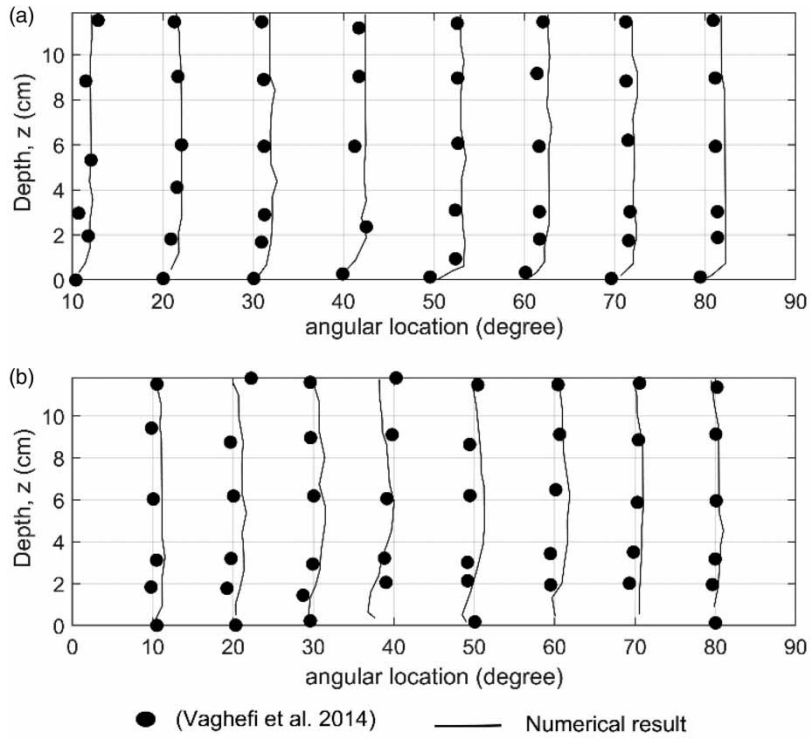

Figure 14 | Comparison of experimental and numerical results of (a) longitudinal velocity; and (b) lateral velocity at a longitudinal section located at 58% of channel width from outer bank of a 90-degree channel bend.

velocity found in the middle of the meander. The direction of velocity gets changed with the inference of spur dyke. This numerical modeling data is very similar to Vaghefi *et al.* (2014). Based on this verification, numerical modeling can be achieved.

Since no experimental investigation was carried out to study the flow pattern around a T-shaped spur dike located in a reverse meandering channel, the experimental results from Vaghefi *et al.* (2014) were used to validate the numerical model. Vaghefi *et al.* (2014) studied the effect of inflow Froude number on flow pattern around the spur dike located at 45-degrees in a 90-degree channel bend using RNG $k - \varepsilon$ model and volume of fluid (VOF). Figure 14 shows the comparison between experimental and numerical velocity results at a longitudinal section located at 58% of channel width, and inflow Froude number equal to 0.34. From the figure, it is clear that there is satisfactory agreement between experimental and numerical data. Hence, it validates the numerical model used in this study.

CONCLUSION

The numerical simulation presented in this paper considering the parameters with and without the spur dyke in the meandering channel has evaluated and analyzed the velocity distribution, streamline, the strength of the secondary flow, bed-shear-stress distribution, and effect Froude number on flow. The results show that the streamline drawn in cross-section persists the two vortices in anti-clock direction and closer to the spur dyke, and these vortices shifted downwards as the strength of the stream gets increased. Since longitudinal pressure is more significant at bend surface and in the absence of spur dyke, this becomes very low. Without the spur dyke in the channel, there is no formation of flow zones, but in contrast with the spur dyke, there is a formation of two velocity zones at the junction of the two bends. Due to the spur dyke, there is the formation of secondary flows, which is maximum at the first bend of the channel; along with it, the maximum bed-shear-stress is formed outside the flow separation zone at the convex tip of the spur dyke. The meander with spur dyke becomes more complicit to protect the heavy flow in the field and helps in damaging the river less. In hydraulics, performing field experiments is very costly and almost impossible to deal with all parameters accurately within the same time. The numerical models are the best way to analyze all parameters, so we hope this numerical investigation helps in the future findings of hydraulics parameters.

DATA AVAILABILITY STATEMENT

All relevant data are included in the paper or its Supplementary Information.

REFERENCES

Acharya, A. & Duan, J. G. 2011 Three-dimensional simulation of flow field around series of spur dikes. In: *World Environmental and Water Resources Congress 2011: Bearing Knowledge for Sustainability*. Palm Springs, CA, USA, pp. 2085–2094.

Fazli, M., Ghodsian, M. & Neyshabouri, S. A. A. S. 2008 Scour and flow field around a spur dike in a 90°bend. *International Journal of Sediment Research* **23** (1), 56–68.

Fluent, A. N. S. Y. S. 2018 *19.2 Theory Guide*. ANSYS. Inc., Canonsburg, PA, USA.

Ghodsian, M. & Vaghefi, M. 2009 Experimental study on scour and flow field in a scour hole around a T-shape spur dike in a 90 bend. *International Journal of Sediment Research* **24** (2), 145–158.

Giri, S., Shimizu, Y. & Surajate, B. 2004 Laboratory measurement and numerical simulation of flow and turbulence in a meandering-like flume with spurs. *Flow Measurement and Instrumentation* **15** (5–6), 301–309.

Jennifer, D. U. A. N., Li, H. E., Guangqian, W. A. N. G. & Xudong, F. U. 2011 Turbulent burst around experimental spur dike. *International Journal of Sediment Research* **26** (4), 471–523.

Jiao, Z. X., Dou, X. P., Zheng, J. H., Zhang, X. Z. & Gao, X. Y. 2017 Influence of spur dike on hydrodynamic exchange between channel and shoal of generalization estuary in physical model test. *China Ocean Engineering* **31** (5), 624–630.

Kafle, M. R. 2013 Numerical simulation of flow around a spur dike with free surface flow in fixed flat bed. *Journal of the Institute of Engineering* **9** (1), 107–114.

Kothyari, U. C. & Ranga Raju, K. G. 2001 Scour around spur dikes and bridge abutments. *Journal of Hydraulic Research* **39** (4), 367–374.

Kuhnle, R. & Alonso, C. 2013 Flow near a model spur dike with a fixed scoured bed. *International Journal of Sediment Research* **28** (3), 349–357.

NajiAbhari, M. N., Ghodsian, M., Vaghefi, M. & Panahpur, N. 2010 Experimental and numerical simulation of flow in a 90 bend. *Flow Measurement and Instrumentation* **21** (3), 292–298.

Olsen, N. R. B. 2018 *A Three-Dimensional Numerical Model for Simulation of Sediment Movements in Water Intakes with Multi-Block Option, User's Manual*.

Ouillon, S. & Le Guennec, B. 1996 Modelling non-cohesive suspended sediment transport in 2D vertical free surface flows. *Journal of Hydraulic Research* **34** (2), 219–236.

Pandey, M., Ahmad, Z. & Sharma, P. K. 2018a Scour around impermeable spur dikes: a review. *ISH Journal of Hydraulic Engineering* **24** (1), 25–44.

Pandey, M., Sharma, P. K., Ahmad, Z., Singh, U. K. & Karna, N. 2018b Three-dimensional velocity measurements around bridge piers in gravel bed. *Marine Georesources&Geotechnology* **36** (6), 663–676.

Pandey, M., Lam, W. H., Cui, Y., Khan, M. A., Singh, U. K. & Ahmad, Z. 2019 Scour around spur dike in sand–gravel mixture bed. *Water* **11** (7), 1417.

Pandey, M., Azamathulla, H. M., Chaudhuri, S., Pu, J. H. & Pourshahbaz, H. 2020 Reduction of time-dependent scour around piers using collars. *Ocean Engineering* **213**, 107692.

Pandey, M., Valyrakis, M., Qi, M., Sharma, A. & Lodhi, A. S. 2021 Experimental assessment and prediction of temporal scour depth around a spur dike. *International Journal of Sediment Research* **36** (1), 17–28.

Pourshahbaz, H., Abbasi, S., Pandey, M., Pu, J. H., Taghvaei, P. & Tofangdar, N. 2020 Morphology and hydrodynamics numerical simulation around groynes. *ISH Journal of Hydraulic Engineering*, 1–9.

Pu, J. H., Pandey, M. & Hanmaiahgari, P. R. 2020 Analytical modelling of sidewall turbulence effect on streamwise velocity profile using 2D approach: a comparison of rectangular and trapezoidal open channel flows. *Journal of Hydro-Environment Research* **32**, 17–25.

Pu, J. H., Wallwork, J. T., Khan, M., Pandey, M., Pourshahbaz, H., Satyanaga, A., Pourshahbaz, H., Satyanaga, A., Hanmaiahgari, P. R. & Gough, T. 2021 Flood suspended sediment transport: combined modelling from dilute to hyper-concentrated flow. *Water* **13** (3), 379.

Radan, P. & Vaghefi, M. 2016 Flow and scour pattern around submerged and non-submerged T-shaped spur dikes in a 90° bend using the SSIIM model. *International Journal of River Basin Management* **14** (2), 219–232.

Rozovski, I. 1957 *Flow of Water in Bends of Open Channels*. Is. Program for Sci. Trans]. Jerusalem.

Salamatian, S. A., Forghani, M. & Tabarestani, M. K. 2016 Flow pattern and stress distribution around three spur dikes in ninety-degree bend. *International Journal of Engineering and Technology* **8** (6), 462–467.

Samadi, M., Jabbari, E., Azamathulla, H. M. & Mojallal, M. 2015 Estimation of scour depth below free overfall spillways using multivariate adaptive regression splines and artificial neural networks. *Engineering Applications of Computational Fluid Mechanics* **9** (1), 291–300.

Samadi, M., Sarkardeh, H. & Jabbari, E. 2021 Prediction of the dynamic pressure distribution in hydraulic structures using soft computing methods. *Soft Computing* **25** (5), 3873–3888.

Sharma, K. & Mohapatra, P. K. 2012 Separation zone in flow past a spur dyke on rigid bed meandering channel. *Journal of Hydraulic Engineering* **138** (10), 897–901.

Singh, U. K., Ahmad, Z., Kumar, A. & Pandey, M. 2019 Incipient motion for gravel particles in cohesionless sediment mixtures. *Iranian Journal of Science and Technology Transactions of Civil Engineering* **43** (2), 253–262.

Singh, R. K., Pandey, M., Pu, J. H., Pasupuleti, S. & Villuri, V. G. K. 2020 Experimental study of clear-water contraction scour. *Water Supply* **20** (3), 943–952.

Spalding, D. B. 1974 The numerical computation of turbulent flow. *Computer Methods in Applied Mechanics and Engineering* **3**, 269.

Vaghefi, M., Shakerdargah, M., Fiouz, A. R. & Akbari, M. 2014 Numerical investigation of the effect of Froude number on flow pattern around a single T-shaped spur dike in a bend channel. *International Journal of Engineering Research* **3** (5), 351–355.

Vaghefi, M., Akbari, M. & Fiouz, A. R. 2016a An experimental study of mean and turbulent flow in a 180-degree sharp open channel bend: secondary flow and bed shear stress. *KSCE Journal of Civil Engineering* **20** (4), 1582–1593.

Vaghefi, M., Yaser, S. & Shaker, H. S. 2016b Effects of distance between the T-shaped spur dikes on flow and scour patterns in 90 bend using the SSIIM model. *Ain Shams Engineering Journal* **7** (1), 31–45.

Vaghefi, M., Ghodsian, M. & Akbari, M. 2017 Experimental investigation on 3D flow around a single T-shaped spur dike in a bend. *PeriodicaPolytechnica Civil Engineering* **61** (3), 462–470.

Vaghefi, M., Radan, P. & Akbari, M. 2019 Flow pattern around attractive, vertical, and repelling T-shaped spur dikes in a mild bend using CFD modeling. *International Journal of Civil Engineering* **17** (5), 607–617.

Xiufang, Z., Pingyi, W. A. N. G. & Chengyu, Y. A. N. G. 2012 Experimental study on flow turbulence distribution around a spur dike with different structure. *Procedia Engineering* **28**, 772–775.

Yakhot, V. S. A. S. T. B. C. G., Orszag, S. A., Thangam, S., Gatski, T. B. & Speziale, C. G. 1992 Development of turbulence models for shear flows by a double expansion technique. *Physics of Fluids A: Fluid Dynamics* **4** (7), 1510–1520.

Yazdi, J., Sarkardeh, H., Azamathulla, H. & Aminuddin, G. 2010 3D -Simulation of flow around single groyne with free surface. *International Journal of River Basin Management, IAHR* **8** (1), 55–62.

Yen, C. L. 1967 *Bed Configuration and Characteristics of Subcritical Flow in A Meandering Channel*.

Zhang, H. & Nakagawa, H. 2008 Scour around spur dyke: recent advances and future researches. 京都大学防災研究所年報. *B=Disaster Prevention Research Institute Annuals. B* **51** (B), 633–652.

First received 1 July 2021; accepted in revised form 25 July 2021. Available online 6 August 2021